Effect of the heating rate on the thermal explosion behavior and oxidation resistance of 3D-structure porous NiAl intermetallic

Materials Characterization 190 (2022) 112062

Contents lists available at ScienceDirect

Materials Characterization

journal homepage: www.elsevier.com/locate/matchar

Effect of the heating rate on the thermal explosion behavior and oxidation resistance of 3D-structure porous NiAl intermetallic

Yang Yu [a], Xiaoping Cai [a,b], Zhejian Cao [c], Xinyang Jiao [d], Weining Xie [e], Yong Yu [a], Peizhong Feng [a,*]

[a] School of Materials Science and Physics, China University of Mining and Technology, Xuzhou 221116, PR China
[b] School of Chemical Engineering and Technology, China University of Mining and Technology, Xuzhou 221116, PR China
[c] Division of Systems and Synthetic Biology, Department of Biology and Biological Engineering, Chalmers University of Technology, 41296 Gothenburg, Sweden
[d] School of Mechanical and Electrical Engineering, Suqian College, Suqian 223800, PR China
[e] Advanced Analysis and Computation Center, China University of Mining and Technology, Xuzhou 221116, PR China

ARTICLE INFO

Keywords:
Porous NiAl intermetallic compounds
3D-XRM
Heating rate
Thermal explosion reaction

ABSTRACT

Porous NiAl intermetallic compounds demonstrate great potential in various applications by their high porosity and excellent oxidation resistance. However, to obtain a controllable NiAl intermetallic structure by tuning different process parameters remains unclear. In this work, porous NiAl intermetallic compounds were fabricated by economic and energy-saving thermal explosion (TE) reaction. The relationship between microstructure and process parameters was revealed using three-dimensional X-ray microscopy (3D-XRM) with high resolution and non-destructive characteristics. The geometrical features and quantitative statistics of the porous NiAl obtained at different heating rates (2, 10, 20 °C min^{-1}) were compared. The result of the closed porosity calculation showed that a lower heating rate (2 °C min^{-1}) promoted the Kirkendall reaction between Ni and Al, resulting in a high closed porosity (5.25%). However, at a higher heating rate (20 °C min^{-1}), a homogeneous NiAl phase was observed using the threshold segmentation method, indicating uniform and complete TE reaction can be achieved at a high heating rate. The result of the 3D fluid simulation showed that the sample heated at 10 °C min^{-1} had the highest permeability (2434.6 md). In this study, we systematically investigated the relationship between the heating rates and properties of the porous NiAl intermetallic, including the phase composition, porosity, exothermic mechanism, oxidation resistance, and compression resistance. Our work provides constructive directions for designing and tailoring the performance of porous NiAl intermetallic compounds.

1. Introduction

Owing to high porosity, stable pore structure, excellent corrosion and oxidation resistance at high temperature, porous Al-based intermetallic compounds (Fe-Al, Cu-Al, Co-Al, Ni-Al) demonstrate promising potential in various applications, such as filtration, purification, flow control. In particular, porous NiAl compounds have become a research hotspot for their excellent heat conduction, oxidation resistance, and weldability [1–8].

Porous NiAl intermetallic compounds can be synthesized by (1) space holder technique (SHT) [9–11], (2) elemental powder metallurgy (EPM) [12–14], (3) combustion synthesis (CS) [15–17]. Compared with SHT and EPM, porous NiAl compounds synthesized by CS possess high porosity and a skeleton structure with connected channels [18–22]. CS can be achieved by two approaches: thermal explosion (TE) and self-propagating high-temperature synthesis (SHS). In the TE approach, the green compact is heated evenly at a steady rate, where the risk of cracking and deformation can be reduced during heating. Up to now, various porous intermetallic compounds (Co-Al, Fe-Al, Ni-Al, Ti-Al, and Ti-Si) have been obtained by the TE approach [23–26].

However, the real combustion temperature of porous NiAl sample during the TE reaction is hard to control. Once the reaction temperature exceeds the melting point of porous NiAl (1638 °C), the compound can melt and lose its structure [27,28]. To solve this problem, Cai et al. [29] proved that the real combustion temperature of porous NiAl can be decreased effectively by extending the holding time, which can effectively suppress the deformation and melting of the product. Jiang et al. [30] studied the effect of heating rate and isothermal treatment on the

* Corresponding author.
E-mail address: fengroad@163.com (P. Feng).

https://doi.org/10.1016/j.matchar.2022.112062
Received 4 May 2022; Received in revised form 12 June 2022; Accepted 13 June 2022
Available online 17 June 2022

sintering of Ni_3Al sample, and concluded that when the sample was treated at a lower heating rate (1–2 °C min^{-1}) to a proper temperature (470–490 °C), the product can maintain its original morphology. Previous studies have made important contributions to the successful preparation of porous NiAl materials, but the effects of sintering parameters on thermodynamics and the oxidation kinetics of sintered products with different heating rates are still unclear.

Three-dimensional X-ray microscopy (3D-XRM) is a powerful tool to analyze porous intermetallic compounds by its high resolution and non-destructive characteristics. While, past research mainly focused on characterizing the three-dimensional porous structure of porous intermetallic compounds, the effect of heating rate on pore distribution and phase composition has not been further studied [31,32].

In this work, porous NiAl intermetallic compounds were obtained by economic and energy-saving TE method. The influence of heating rate on the macroscopic morphology, exothermic mechanism, microstructure, oxidation resistance and mechanical properties of porous NiAl were investigated. Moreover, 3D-XRM was used to study the pore distribution with different heating rates. This study offers a fundamental understanding of the pore formation mechanism and the effect of heating rate on porosity in porous intermetallic compounds.

2. Materials and experimental methods

2.1. Raw materials and preparation process

Ni powders (Shanghai Aladdin Biochemical Technology Co., Ltd., 75 μm, 99.9% purity), Al powders (Shanghai Aladdin Biochemical Technology Co., Ltd., 38–75 μm, 99.9% purity) were proportionately mixed in a roller mixer (Mixer-RM1, 200 rpm for 24 h). The atomic ratio of porous NiAl was Ni-50 at.% Al. A stainless-steel mold was used to obtain the columnar green compact with a diameter of 1.5 cm and height of 0.2–0.3 cm. The applied pressure was 300 MPa and the holding time was 5 min. Subsequently, the green compacts were heated to 700 °C with a series of heating rates (2, 5, 10, 12, 15, 20 °C min^{-1}) in a tube furnace (OTF-1200X, China) under H_2 atmosphere (200 mL m^{-1}, 99.99%). After the furnace cooled to the room temperature, obtained samples were transferred out of the furnace.

The oxidation experiment was carried out in a muffle furnace (KSL-1500X, China) at 900 °C under air atmosphere. The mass change of porous NiAl was recorded after the set oxidation time. Based on formula (1), the functional relationship between mass change and oxidation time was used to evaluate the oxidation kinetics laws.

$$M_G = (m_t - m_0)/m_0 \times 100\% \quad (1)$$

M_G is the mass change of porous NiAl after a certain oxidation time, m_t is the mass of porous NiAl after different oxidation time, m_0 is the initial mass of porous NiAl before oxidization.

With crosshead speed of 1 mm min^{-1}, an electronic universal testing machine (UTM 5305, China) was used for the compression resistance test. Three samples with the same size were tested to calculate the average compressive strength under each heating condition.

2.2. Materials characterization

Differential scanning calorimeter (DSC, F5-Jupiter STA449, Netzsch, Germany) was used to analyze the heat change of the compounds during the TE reaction. The samples were heated up to 700 °C with a series of heating rates (2, 5, 10, 20 °C min^{-1}). To prevent oxidation, a consecutive Ar flow was used during the DSC test.

The phase composition of porous NiAl was identified by X-ray diffraction characterization (Bruker D8 Advance, using Cu target with $\lambda = 0.154184$ nm). Filed-emission scanning electron microscopy (FE-SEM, SU8220, Japan) coupled with the function of Energy Dispersive Spectroscopy was applied for investigating the microstructure and element composition.

Three-dimensional X-ray microscopy (3D-XRM) was used to analyze the pore size and phase distribution of porous NiAl. High resolution (≈ 0.7 voxels) 3D images of porous NiAl were obtained by Zeiss™ Xradia Versa 510 X-Ray Microscope. The scanning voltage was set to 80 kV, and the corresponding scanning current was 88 μA. For samples with three heating modes (2, 10, 20 °C min^{-1}), in the exposure time of 6 s, 3001 projections were taken within 360°, and the average pixel size was 1.909 μm. InspeXio (Shimadzu Co., Ltd., Japan) was used to reconstruct the 2D images into 3D models. The software of Dragonfly (ORS Inc., Canada) and Avizo (VSG Inc., Burlington, MA, USA) were used for threshold segmentation, fluid simulation and other postprocessing work. The schematic of 3D-XRM, image processing, and 3D reconstruction were illustrated in Fig. 1.

3. Results and discussion

3.1. Phase composition and microstructure

Fig. 2 shows the effect of heating rate on the macroscopic morphology of NiAl sintered pellets. All sintered pellets show obvious volume expansion compared to the green compact. The expansion rate increases with the increasing of the heating rate (2–10 °C min^{-1}). However, when the heating rate continues to increase (10–20 °C min^{-1}), the expansion rate decreases gradually. Besides, the melting and deformation also occur at the edge of the product. This could be explained by that the high heating rate promotes TE reaction, where a large amount of heat releases instantly and results in the melting and deformation in porous NiAl [33]. By comparison, 10 °C min^{-1} is the best parameter for obtaining stable porous NiAl product.

In order to further study the effect of heating rate on porous NiAl, four heating modes (2, 5, 10 and 20 °C min^{-1}) are selected as the research objects. Fig. 3 shows the DSC curves of NiAl samples heated from 20 °C to 700 °C with a series of heating rates. Each curve shows two exothermic peaks in the range of 400–700 °C. The first exothermic peak is due to the interdiffusion reaction between Ni and Al, corresponding to the process of solid-state diffusion, which has the characteristics of a wide temperature range and weak intensity [34]. With the heating rate increasing from 2 °C min^{-1} to 10 °C min^{-1}, the initial temperature (T_{im}) of the first peak increases from 558 °C to 568 °C, and the continuous temperature range (T_{fm}-T_{im}) gradually decreases. Apart from that, the thermal effect of the first peak decreases from 158.1 J g^{-1} to 53.0 J g^{-1} and the peak gradually tends to be flat. Notably, when the heating rate increases to 20 °C min^{-1}, the first peak has completely disappeared. In fact, the diffusion reaction between Ni and Al can be fully completed at a lower heating rate, resulting in more diffusion heat release. When the heating rate gradually increases, there is not enough time for the interdiffusion reaction, but directly reaches the melting point of Al (660 °C), therefore the heat released by diffusion reaction is reduced. The second exothermic peak is due to the violent TE reaction, and it is sharper and narrower than the first peak [34]. Notably, the temperature range from the initial temperature to the peak temperature (T_{pr}-T_{ir}) gradually decreases with the increasing of the heating rate. The thermal effect of the second peak gradually increases from 163.5 J g^{-1} to 637.0 J g^{-1}, illustrating the increase of the heating rate promotes the melting of Al and accelerates the TE reaction. In general, a low heating rate is conducive to the interdiffusion reaction of porous NiAl, and a high heating rate would promote the TE reaction. Cai et al. [29] concluded the first peak can block the second peak, which reduced the heat in the TE reaction. In the Ni-Al system, decreasing the heating rate can suppress melting and deformation of the products that caused by violent TE reaction, while a low heating rate might be more energy- and time-consumption.

The SEM images of the sintered porous NiAl, as shown in Fig. 4, demonstrate the influence of heating rates on the microstructure of porous NiAl. From Fig. 4a, when the sample is heated at 2 °C min^{-1}, a weak TE reaction leads to only a small amount of TE pores distributed in

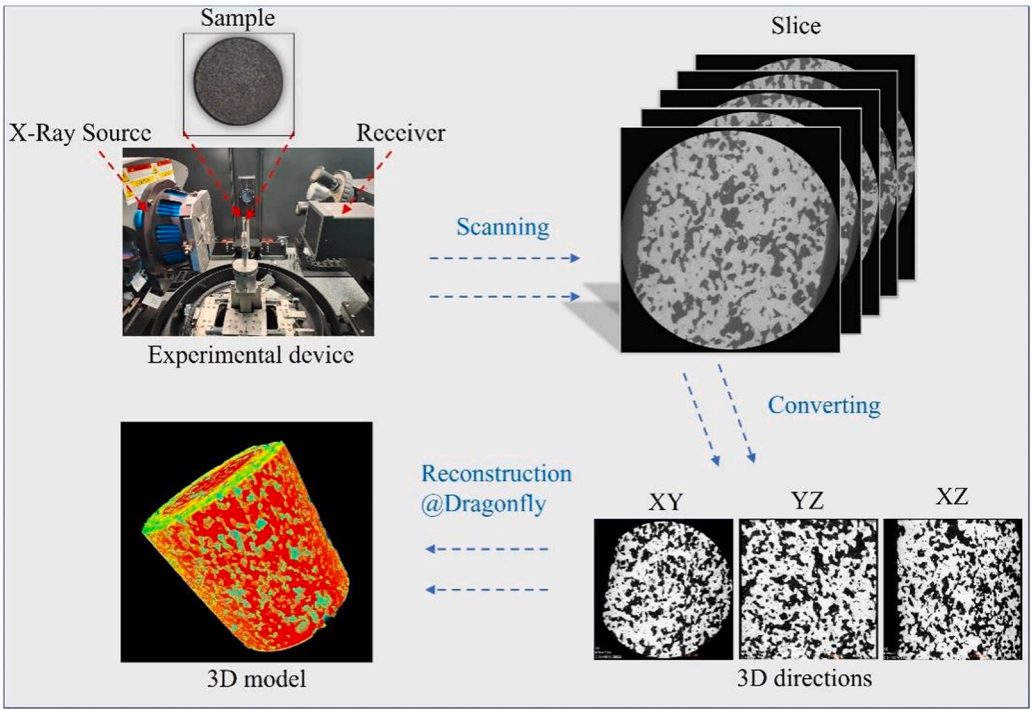

Fig. 1. Process of 3D-XRM data acquisition and 3D reconstruction.

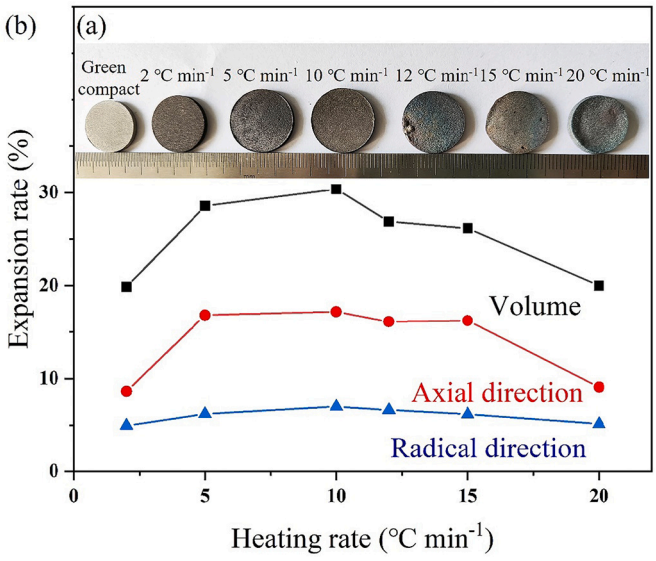

Fig. 2. Influence of heating rate on the macroscopic morphology of porous NiAl pellets. (a) green compact and sintering products with different heating rates, (b) functional relationship between heating rate and expansion rate based on radical direction (blue curve), axial direction (red curve), and volume (black curve). (For interpretation of the references to color in this figure legend, the reader is referred to the web version of this article.)

the sintering product. Besides, low heating rates promote the interdiffusion reaction, which can produce some closed pores. Fig. 4(a1) shows the skeleton structure of the porous NiAl with the heating rate of 2 °C min^{-1}, the particles are relatively small and closely arranged with each other, and many small closed pores exist in the skeleton. From Fig. 4a-c, the number of TE pores increases with the increasing of the heating rate, and the skeleton particles become larger in a smoother skeleton. When the heating rate increases to 20 °C min^{-1}, the melting parts can block the pores, and the number of pores decreases. When heated at a low heating rate, diffusion reaction between Ni and Al can finish completely and the particles have enough time to grow up and closely combined. Therefore, many small closed pores are formed between particles. While, the heating rate gradually increases to 20 °C min^{-1}, Al changes rapidly from solid to liquid, and reacts violently with Ni particles. The adhesion of particles is relatively loose and a lot of small pores are generated [34]. However, excessive heating rate (20 °C min^{-1}) can lead to the melting and deformation, which is not conducive to obtain products with high porosity. Fig. 5 shows the cross-section of porous NiAl at a low heating rate. Besides NiAl phase, a large amount of unreacted Ni can be observed in the product, which also proves that a low heating rate can effectively inhibit the TE reaction.

Fig. 6 exhibits XRD results of porous NiAl heated to 700 °C with a series of heating rates. When heated at 2 °C min^{-1}, besides NiAl and Ni phases, the product also contains Ni_2Al_3 mesophase, which is generated by the interdiffusion reaction [35]. With the heating rate increasing, the peak of Ni_2Al_3 and Ni phases decrease gradually, and only NiAl phase exists in the product. From Fig. 6 (b), when the heating rate is 2 °C min^{-1}, Ni, Ni_2Al_3 and NiAl phases can be detected. Due to the relatively weak TE reaction, Ni cannot react with Al completely [36]. When the heating rate increasing from 5 °C min^{-1} to 20 °C min^{-1}, the full width at half maximum (FWHM) of NiAl decreases, which proves the grains size increases with the increasing of the heating rate.

To explore the influence of heating rate on the diffusion reaction of porous NiAl, Fig. 7 shows the cross-section morphology of porous NiAl, which are heated from 20 °C to 630 °C with a series of heating rates. When the samples are heated to 630 °C, all samples contain Ni, Ni_2Al_3 and Al phases (as shown in Fig. 7(g-i)). NiAl phase is not found, which proves only diffusion reaction occurs before 630 °C. The result is consistent with Fig. 3. Then, the thickness change of Ni_2Al_3 diffusion layer is shown in Fig. 7(a-d). The thickness of Ni_2Al_3 is 8.25 μm when heated at 2 °C min^{-1} and the distribution of Ni_2Al_3 is relatively uniform. With the heating rate increasing to 20 °C min^{-1}, the thickness of the diffusion layer decreases to 3.84 μm. In fact, when the sample is heated at a relatively low heating rate, the change of heat is relatively low. There is sufficient time for diffusion reaction between Ni and Al, and the thickness of Ni_2Al_3 is uniform [29]. While, when the sample is heated at

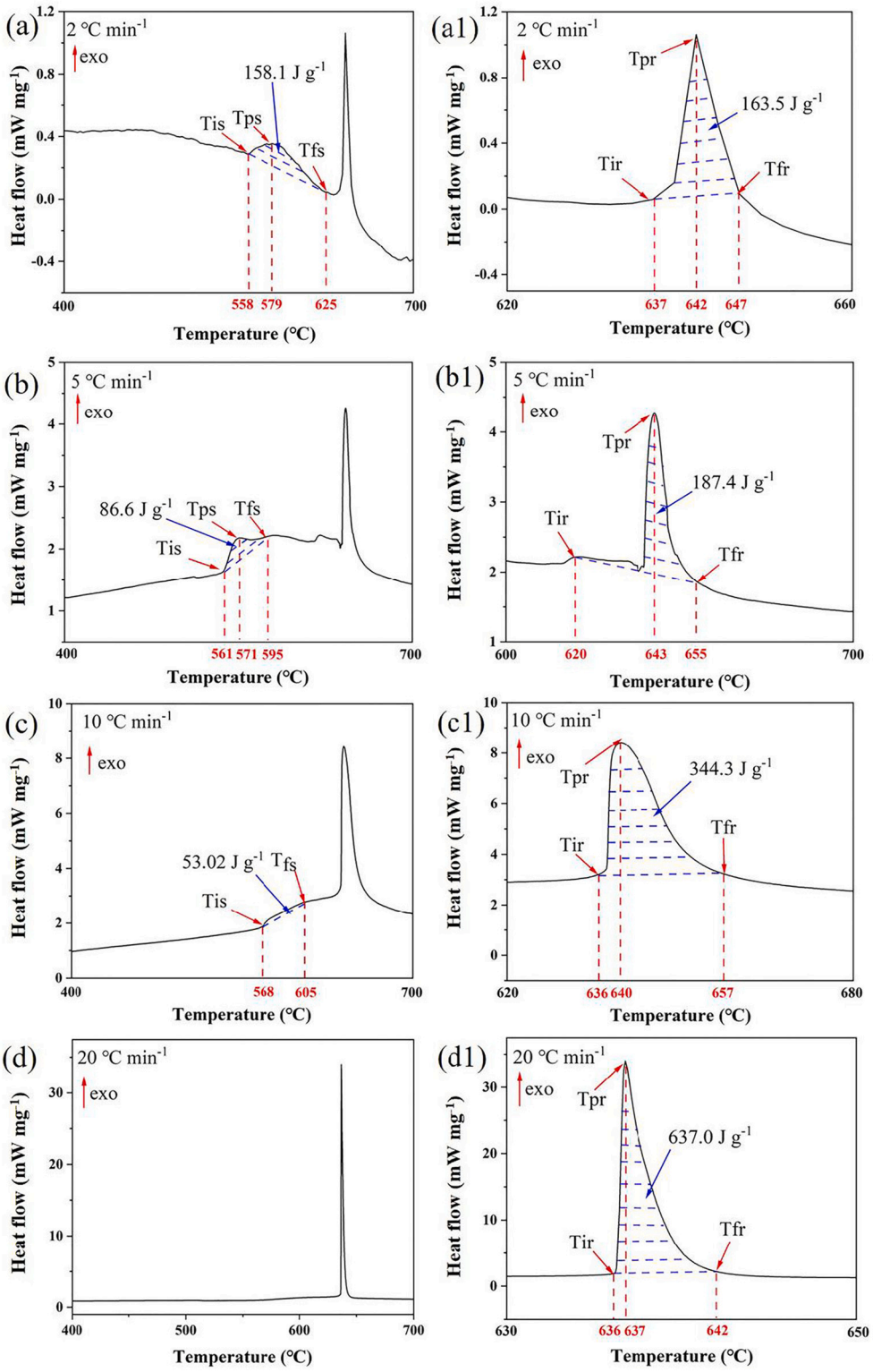

Fig. 3. DSC curves of porous NiAl at different heating rate: (a) 2 °C min^{-1}, (b) 5 °C min^{-1}, (c) 10 °C min^{-1} and (d) 20 °C min^{-1}. (a1)-(d1) corresponding zoom-in curves in the range of 600–700 °C.

a high heating rate, there is not enough time for diffusion reaction between Ni and Al, and TE reaction would directly occur. Therefore, only a small amount of mesophase appears in Fig. 7d. Jiao et al. [37] proposed that Kirkendall pores were due to the diffusion reaction between elements, and a low heating rate promoted the formation of Kirkendall pores (as shown in Fig. 7e). The connected pores (Fig. 7f) are produced due to the violent TE reaction.

3.2. *Three-dimensional structure analysis*

The phase distribution and real pore structure of porous materials are characterized by 3D-XRM, without destroying the specimen. The porosity and pore size of the sample can be calculated quantitatively by Three-Dimensional Reconstruction Software, which is a practical tool to analysis porous intermetallic compounds [38–42].

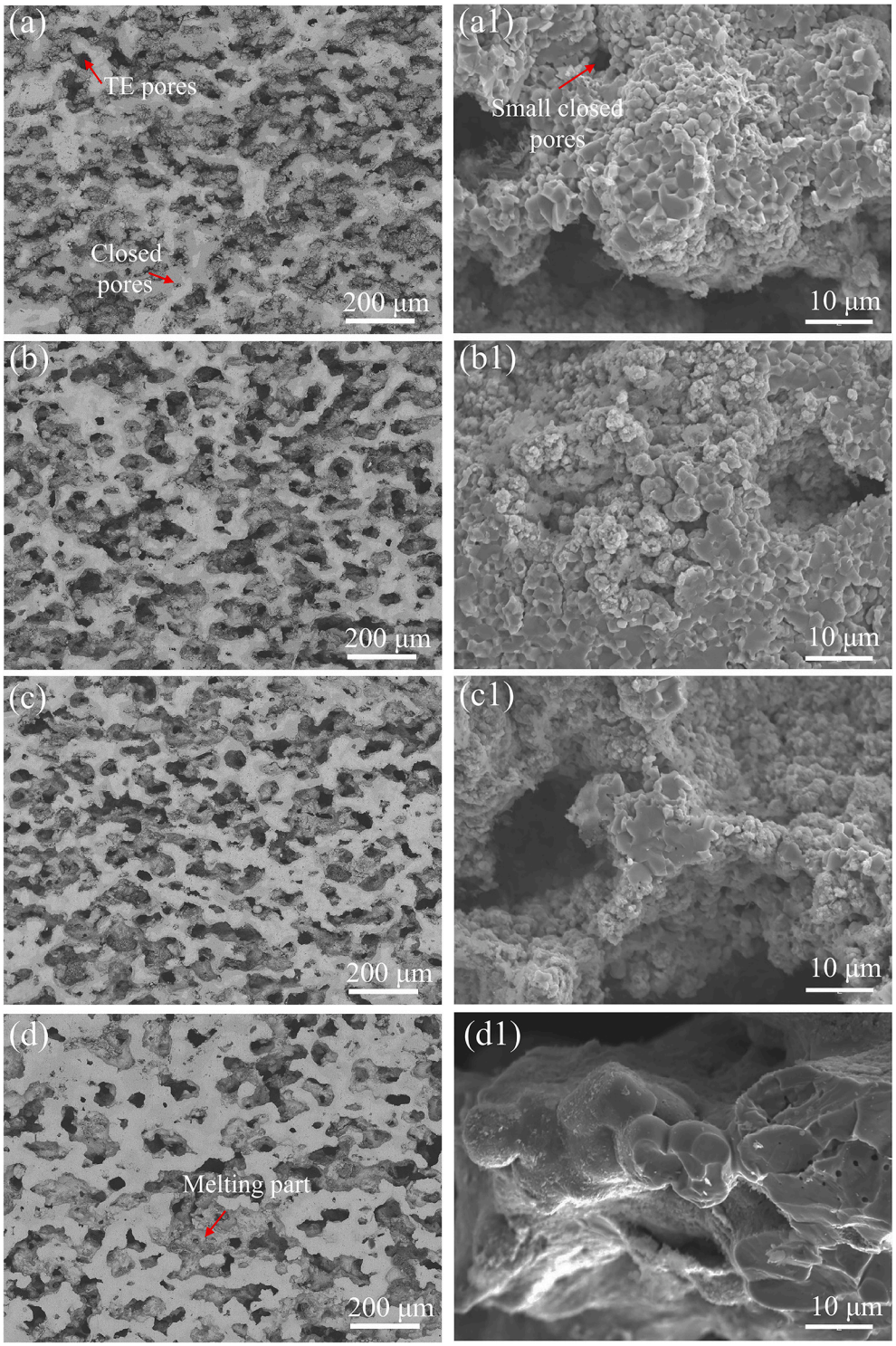

Fig. 4. SEM images of porous NiAl pellets at 700 °C with different heating rates (2, 5,10 and 20 °C min^{-1}). (a-d): the polished section of the porous NiAl. (a1-d1): the skeleton structure of porous NiAl.

To display the influence of the heating mode on the pore and phase distribution in the porous NiAl from 3D perspective, four fixed height slices are used as representative areas: (I-IV), as shown in Fig. 8. In Fig. 8, the low X-ray absorption region represents the pores (the black areas), and high X-ray absorption region represents different phase compositions of porous NiAl (the white and grey areas). By comparing four slices in three modes separately, the pores and phases are found evenly distributed in the product. In the TE mode, porous NiAl is evenly heated and produces a large number of pores.

In Fig. 9, slice (I) in three modes is selected to investigate the influence of heating mode on pore distribution and phase composition. After heated at 2 °C min^{-1}, a large amount of unreacted Ni can be found in the sintering product. This is mainly due to the low degree of the TE reaction. Solid Ni cannot react completely with liquid Al, which conforms to the result of XRD in Fig. 6 [29]. From region 2 in (b-I), the Kirkendall pores produced by interdiffusion reaction between elements that exist in the skeleton of porous NiAl intermetallic compounds, and the connecting pores produced by TE reaction evenly distribute in the

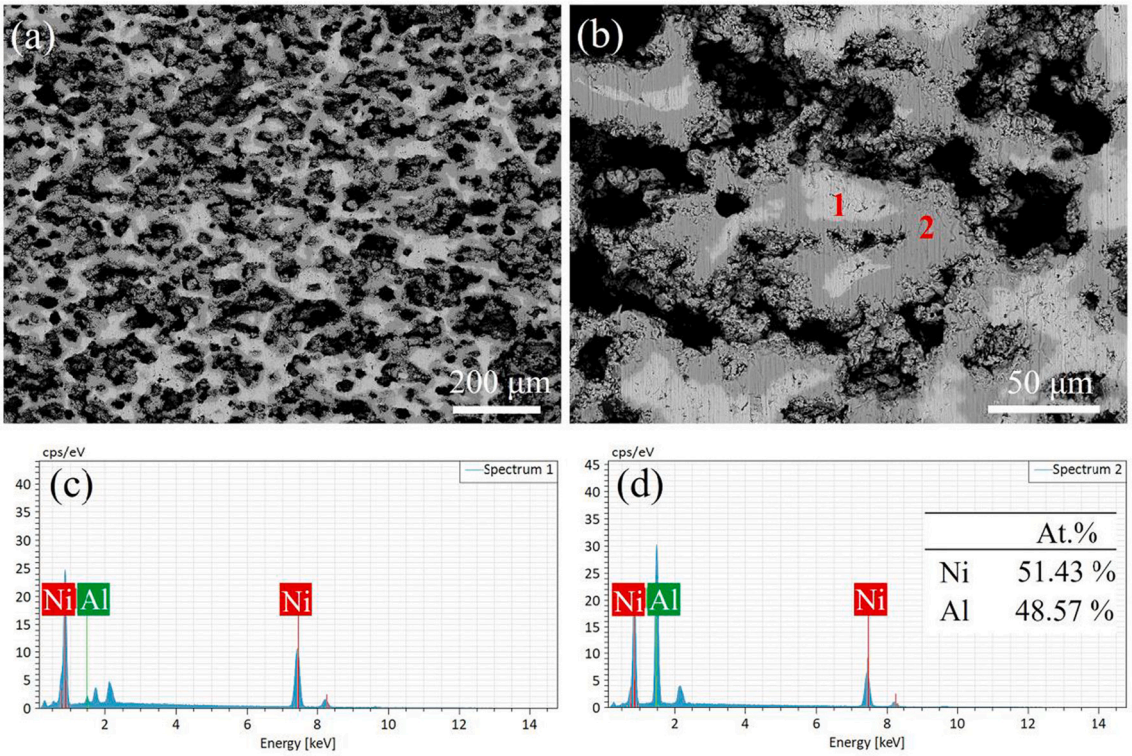

Fig. 5. The SEM images of the cross-sections of porous NiAl compacts heated to 700 °C at 2 °C min^{-1}, (a) at low-magnification, (b) at high-magnification. (c) and (d) EDS patterns of points 1 and 2 marked in Fig. 5 (b).

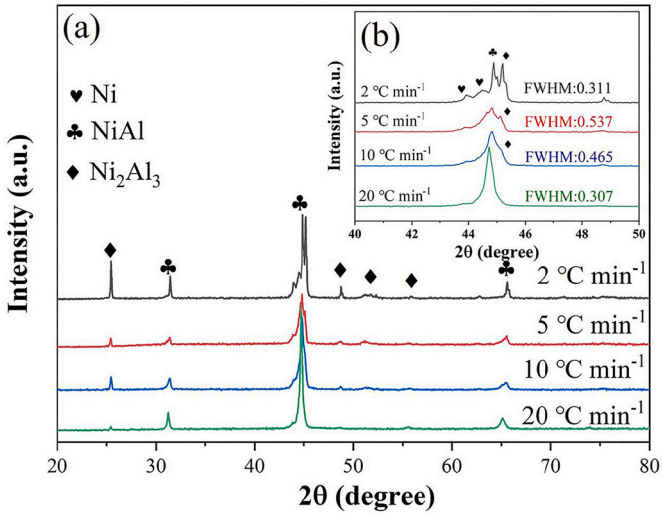

Fig. 6. The influence of heating rate on phase composition of porous NiAl. (a) XRD patterns of porous NiAl heated to 700 °C with different heating rates. (b) zoom-in images in the range of 40°- 50°.

product [43]. When the sample is heated in mode 3, the phase composition of the product is NiAl without other mesophases, which proves that pure porous NiAl intermetallic compounds can be obtained at a high heating rate. However, from region 3 in (a-I), the melting part can be found in the product, which is in coordination with the Fig. 2.

3D-XRM can distinguish the phase composition of NiAl intermetallic compounds by the color change caused by the difference of X-ray absorptivity. The result of threshold segmentation with unreacted Ni of mode 1 and mode 2 is shown in Fig. 10. The yellow areas are unreacted Ni, the black areas are pores and the grey areas are NiAl phase. When heated at 2 °C min^{-1}, some unreacted Ni exists in the product due to weak TE effect, and its volume fraction is 9.62%. With the heating rate increasing to 20 °C min^{-1}, TE reaction is promoted, more melting Al react with solid Ni, and the volume fraction of unreacted Ni decreases to 6.47%. Significantly, the line graph shows the local volume distribution of the unreacted Ni of the samples in the Z direction, and it proves the unreacted Ni is evenly distributed in the samples. Notably, mode 3 has extremely little unreacted Ni because of the violent TE reaction, which is unable to calculate the result accurately.

The pores distribution and the total porosity of the products under three heating modes are shown in Fig. 11. The red areas are pores, and the white areas are skeleton of the sample. From Fig. 8 and Fig. 9, the pores are evenly distributed in three samples, and mainly exist in the form of connecting pores, which exhibits the characteristic of high porosity in porous NiAl intermetallics. By comparing the slice (I) in three modes, the product in the mode 2 has the highest total porosity of 57.31%. Meanwhile, the total porosity of mode 1 is 46.23% with the weak TE reaction. The total porosity of the sample in mode 3 condition is only 39.92% for the plugging effect of melting and deformation on pores at high heating rate.

After TE reaction, porous NiAl mainly exists three kinds of pores: (1) interstitial pores in the green compact, (2) Kirkendall pores caused by elements interdiffusion effect, (3) connecting pores produced by TE reaction. Among them, Kirkendall pores and interstitial pores are closed pores. To investigate the influence of the heating rate on the closed pores, deep learning tool is used to calculate the porosity, the results are shown in the Fig. 12. The blue areas are closed pores, the black areas represent connecting pores, and the grey areas are skeleton. By comparing the slice (I) in three modes, the product in the mode 1 with the highest closed porosity, which can reach 5.25%. Actually, the mainly reaction between Ni and Al is interdiffusion reaction at a low heating rate, producing a large number of Kirkendall pores. When in the mode 3, there is not enough time for the interdiffusion reaction between Ni and Al, while the violent TE reaction directly happens and the closed

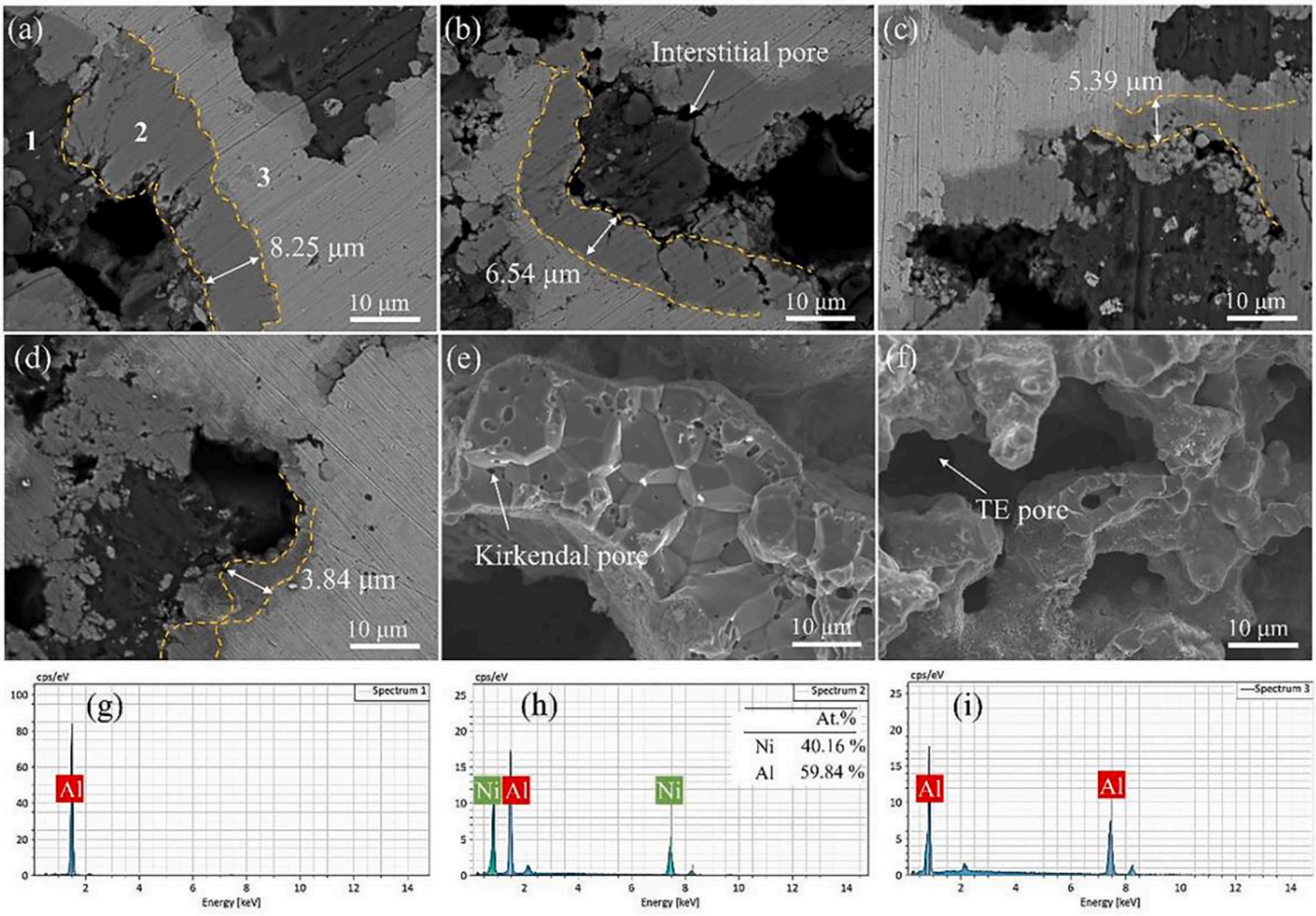

Fig. 7. The cross-section morphology of porous NiAl compacts in 630 °C with different heating rates: (a-d) 2, 5, 10, 20 °C min^{-1}. The fractured morphology of porous NiAl in 630 °C with the heating rate of: (e) 2 °C min^{-1}, (f) 20 °C min^{-1}. (g-i) EDS patterns and element composition of point 1, 2 and 3 marked in Fig. 7 (a).

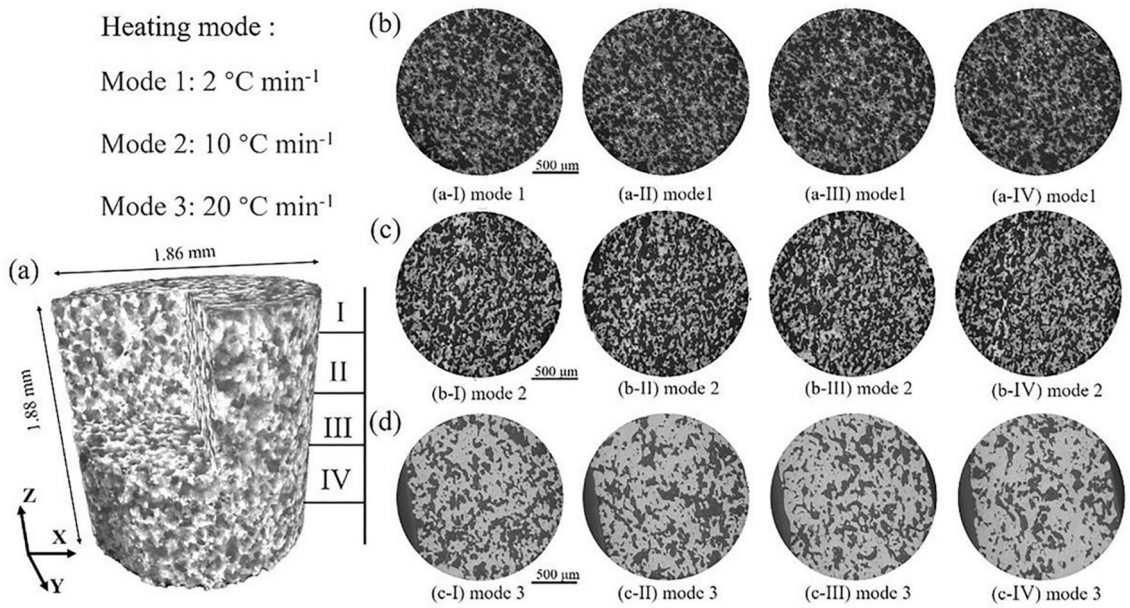

Fig. 8. Scanned and reconstructed results of porous NiAl: (a) The 3D reconstruction model of porous NiAl. Cross-sectional view of porous NiAl heated to 700 °C in different heating modes: (b) 2 °C min^{-1}, (c) 10 °C min^{-1} and (d) 20 °C min^{-1}.

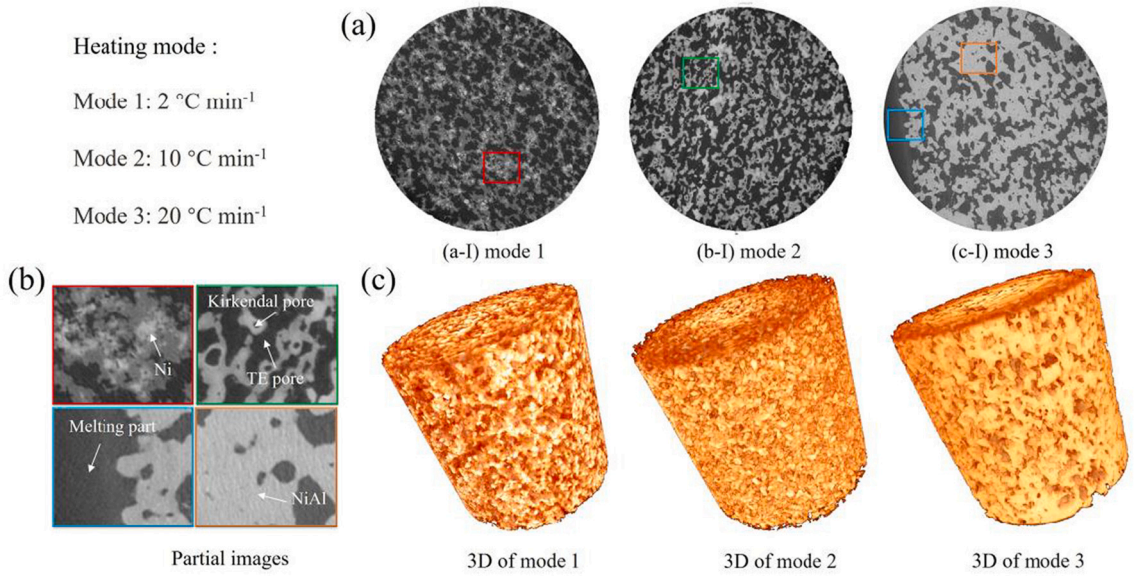

Fig. 9. The influence of heating mode on phase distribution and pore characteristics of porous NiAl: (a) exemplary slice diagrams from three heating modes. (b) partial images in Fig. 9 (a). (c) 3D morphology of porous NiAl in three heating modes.

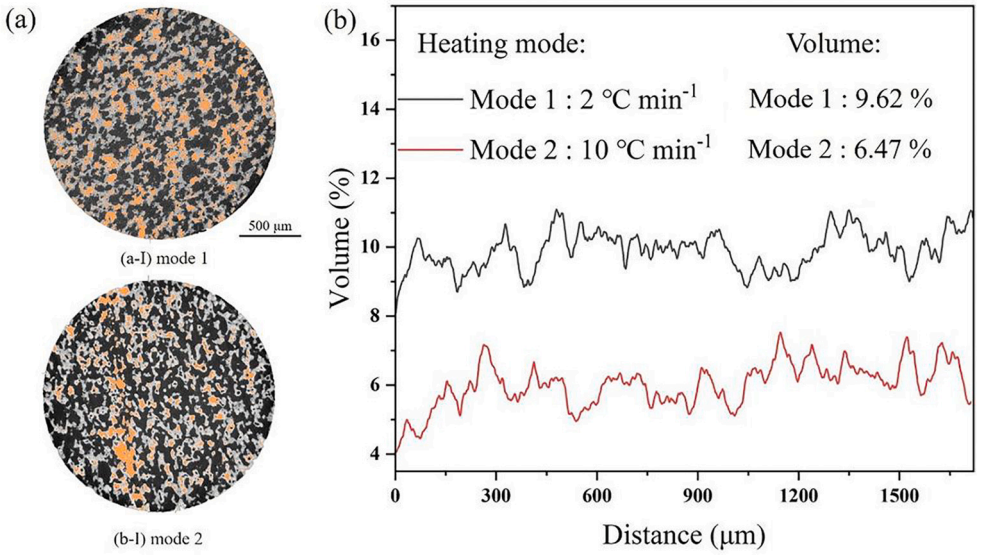

Fig. 10. The result of threshold segmentation in porous NiAl after TE reaction: (a) the distribution of unreacted Ni in porous NiAl with the heating mode 1 and 2. (b) the volume of unreacted Ni in porous NiAl are measured on XY slices perpendicular to the Z direction.

porosity in the mode 3 is only 2.71%. To verify the accuracy of the results of image analysis, the Archimedes principle is also used to calculate the closed porosity. The closed porosity measured by Archimedes principle are 5.03% (Mode 1), 3.11% (Mode 2) and 2.56% (Mode 3), respectively, which is similar to the results of image analysis.

Fig. 13 shows the result of fluid simulation in different heating modes. The colored lines can clearly reflect hundreds of flow routes of porous NiAl. From mode 1 to mode 2, the streamline distribution tends to be uniform, the number of the streamlines also increases. The permeability increases from 2048.2 md to 2434.6 md with the heating rate increasing to 10 °C min^{-1}. This is mainly due to high heating rate leads to more violent TE reaction, more pores are produced and eventually forming the flowing channels. From mode 2 to mode 3, the streamlines are significantly reduced and unevenly distributed, the permeability decreases from 2434.6 md to 1738.8 md. This is mainly because excessive violent TE reaction leads to melt and deformation of the samples, the seepage channels decreasing.

3.3. Oxidation resistance

Porous NiAl materials have good oxidation resistance at high temperature, which can form a dense Al_2O_3 layer at high temperature to prevent the reaction between air and matrix. The effects of composition and temperature on its high-temperature oxidation resistance have been researched [29]. In this work, the high-temperature oxidation resistance of porous NiAl with different heating rates was studied, and the oxidized samples were named OS-2 (2 °C min^{-1}), OS-5 (5 °C min^{-1}), OS-10 (10 °C min^{-1}) and OS-20 (20 °C min^{-1}).

Fig. 14 shows the mass gain curves of sample after being oxidized at 900 °C for 120 h in air atmosphere, which illustrates the oxidation kinetics of porous NiAl. All samples follow the parabolic oxidation rate law, and present a continuous slow increasing trend. Significantly, the

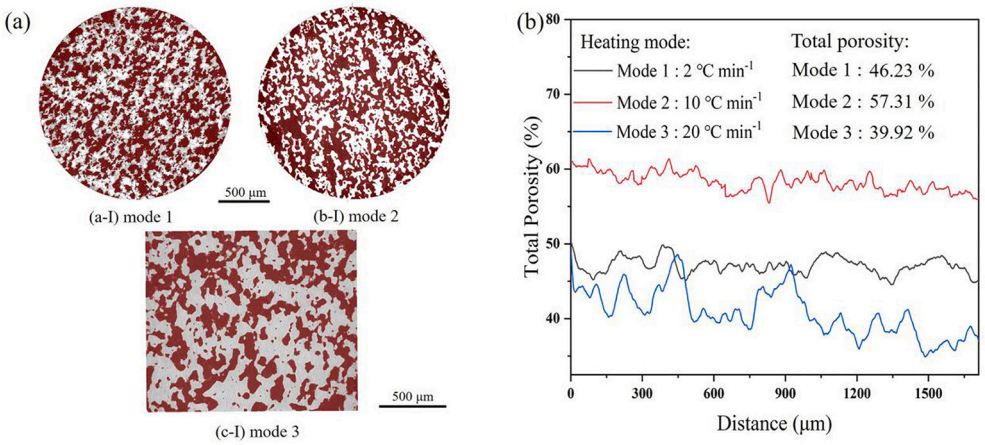

Fig. 11. The result of threshold segmentation in porous NiAl after TE reaction: (a) the distribution of pores in porous NiAl with different heating modes. (b) the total porosity of porous NiAl is measured on XY slices perpendicular to the Z direction.

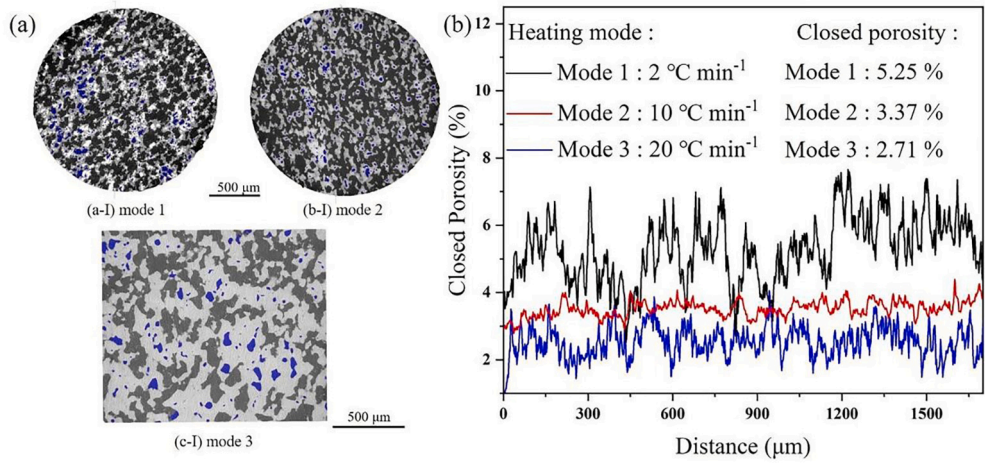

Fig. 12. The result of threshold segmentation in porous NiAl after TE reaction: (a) the distribution of closed pores in porous NiAl with different heating modes. (b) the closed porosity of porous NiAl is measured on XY slices perpendicular to the Z direction.

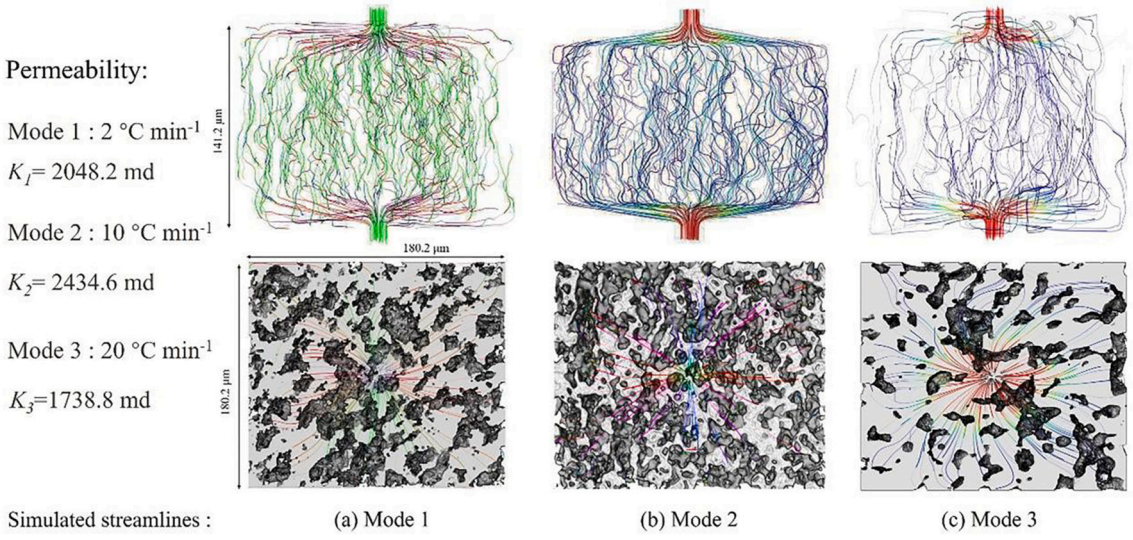

Fig. 13. Effect of heating mode on streamline distribution and permeability of porous NiAl.

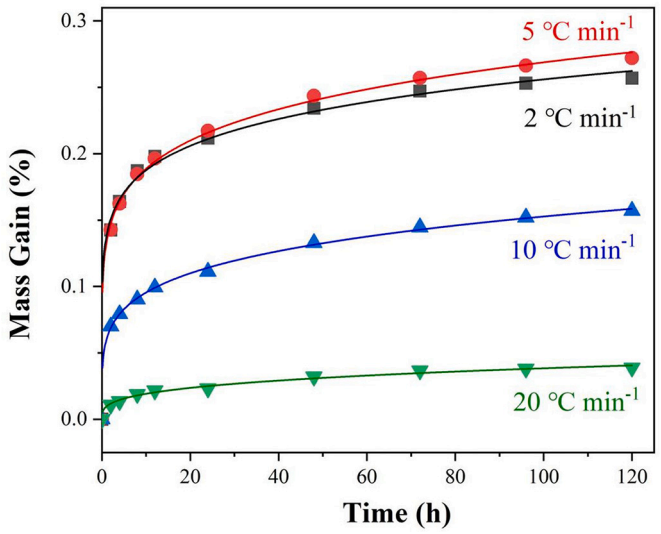

Fig. 14. Mass gain during cyclic exposure of porous NiAl at 900 °C for 120 h in air atmosphere.

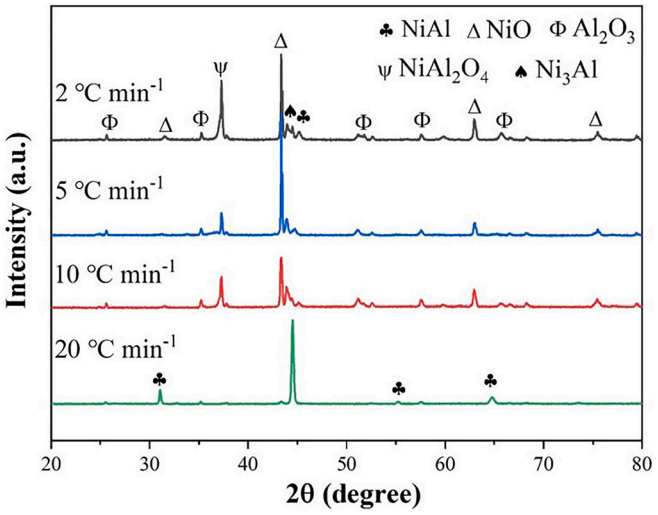

Fig. 15. XRD patterns of the oxidation products of porous NiAl at 900 °C for 120 h.

mass gain of OS-20 is only 3.87%, while, the mass gain of OS-2, OS-5 is 25.7% and 27.2%, which shows relatively rapid quality growth trends. When porous NiAl is heated at a low heating rate (2, 5 °C min^{-1}), weak TE reaction leads to a large amount of unreacted Ni in the sintering product. In the oxidation process, unreacted Ni tends to react with O_2 to form NiO, which leads to a rapid increase in the mass of oxidation product. When the sample is heated at 10 °C min^{-1}, the sintered product has the highest porosity (57.31%). However, high porosity provides more channels for O_2 to contact the internal matrix. After oxidation at 900 °C for 120 h, the mass gain of OS-10 can still reach 14.01%. While, high heating rate promotes the TE reaction, and can obtain uniform porous NiAl materials. Due to the low porosity (39.92%) and uniform NiAl phase, OS-20 has minimal mass gain.

To explore the relationship between the heating rate and oxidation kinetics, the Wagner rate law is used to investigate the parabolic rate law [44]:

$$\left(\frac{\Delta m}{m_0}\right)^2 = k_p t \tag{2}$$

Δm represents the mass change in the oxidation process, m_0 represents the mass of unoxidized sample, kp and t represent the parabolic law constant and the oxidation time, respectively. Table 1 shows the effect of the heating rate on the rate constants and measurement coefficients in the oxidation process. The Parabolic rate constants and measurement coefficients R^2 of different oxidation products are shown in Table 1.

The phase composition of the oxidation products of porous NiAl are shown in Fig. 15. The phase composition of OS-2 is complex, which contains a mixture of NiO, Al_2O_3 and $NiAl_2O_4$, etc. While, compared with OS-2, the phase composition of OS-20 is relatively single, only a small amount of Al_2O_3 can be detected. From Fig. 5, the sintering product with low heating rate exists a lot of unreacted Ni, which can react with O_2 in the oxidation process and lead to severe oxidation in the matrix of porous NiAl. When porous NiAl is heated at a high heating rate, the violent TE reaction completes instantly, the product is pure porous NiAl, which has excellent high-temperature oxidation resistance. The oxidation reactions of OS-2 can be written as:

$$Ni(s) + 1/2O_2(g) \rightarrow NiO(s) \tag{3}$$

$$NiO(s) + Al_2O_3(s) \rightarrow NiAl_2O_4(s) \tag{4}$$

$$NiAl(s) + 1/2O_2(g) \rightarrow 1/3Ni_3Al(s) + 1/3Al_2O_3(s) \tag{5}$$

To further investigate the thickness of the oxide layer of porous NiAl, SEM and EDS analysis of the oxidation products are shown in Fig. 16. Except OS-2, other oxidation products have a continuous and dense Al_2O_3 layer, and the thickness of Al_2O_3 layer decreases with the increasing of the heating rate. When the sample is heated at 2 °C min^{-1}, there is a large amount of unreacted Ni in the sintering product, which is easy to react with O_2 to form NiO, and cannot form the continuous Al_2O_3. NiO can be found in Fig. 17a, while other oxidation products almost have no NiO, only NiAl matrix and a small amount of Al_2O_3 exist in Fig. 17(a-c).

For porous NiAl materials, the connected and uniform pores can significantly improve the filtration flux. While, the increase of porosity would lead to the thinning of pore wall, resulting in the decline in mechanical properties. Fig. 18 shows the effect of heating rate on stress-strain curve of porous NiAl. All samples show obvious elastic deformation zone and fracture zone when samples are heated from 20 °C to 700 °C, which shows the characteristics of brittle fracture of porous NiAl. For brittle materials, the stress of the fracture point is corresponding to compressive strength [45]. When heated at 20 °C min^{-1}, the compressive strength of porous NiAl is 92.8 MPa, reaching the maximum value. The compressive strength of the product heated at 10 °C min^{-1} is relatively weak, only 47.5 MPa. According to the above analysis, the increase of heating rate promotes the TE reaction, therefore the total porosity is increasing and the mechanical properties are weakening. While, porous NiAl is prone to melting and deformation once the heating rate is too fast. The pores are blocked and the bonding strength between particles is improved, which have better mechanical properties [46,47].

Table 1
Oxidation rate constants and measurement coefficients R^2 of the oxidation process (0−120h).

Porous NiAl	Oxidation stage	
	Parabolic rate constant (K_1/%^{2}•h^{-1})	R^2
2 °C min^{-1}	2.519×10^{-5}	0.970
5 °C min^{-1}	1.008×10^{-5}	0.991
10 °C min^{-1}	2.589×10^{-6}	0.995
20 °C min^{-1}	2.340×10^{-6}	0.960

4. Conclusions

Porous NiAl was successfully fabricated by economical and energy-saving TE reaction. The influence of heating rates on the phase composition, porosity, exothermic mechanism, oxidation resistance and

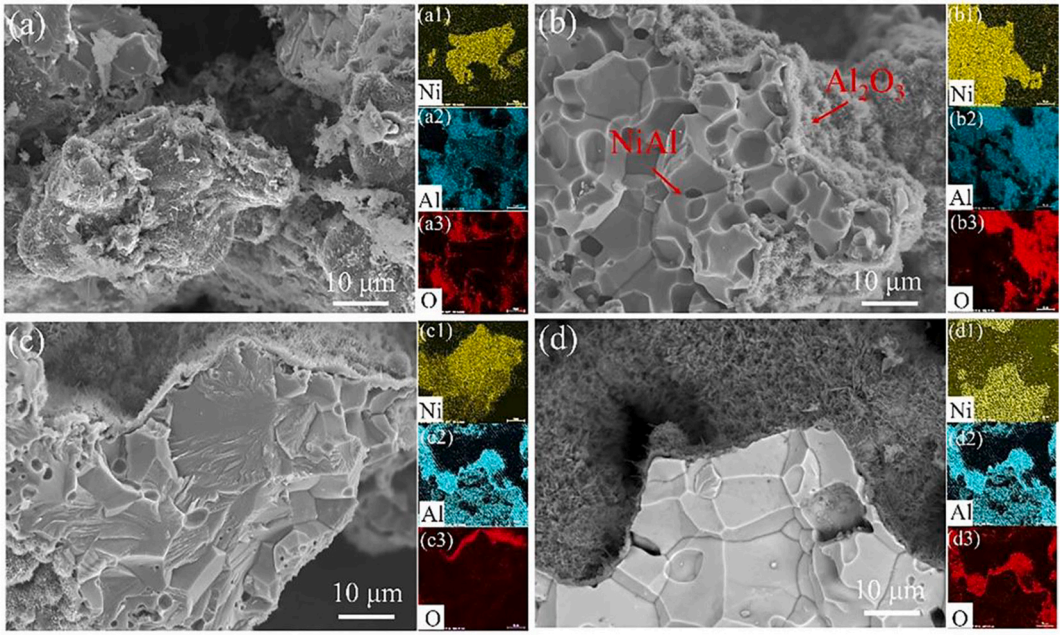

Fig. 16. SEM and EDS images of the fractured morphology of the oxidized products. (a)-(d) the oxidation product of OS-2, OS-5, OS-10 and OS-20. (a1-d3) mapping distribution of overall elements.

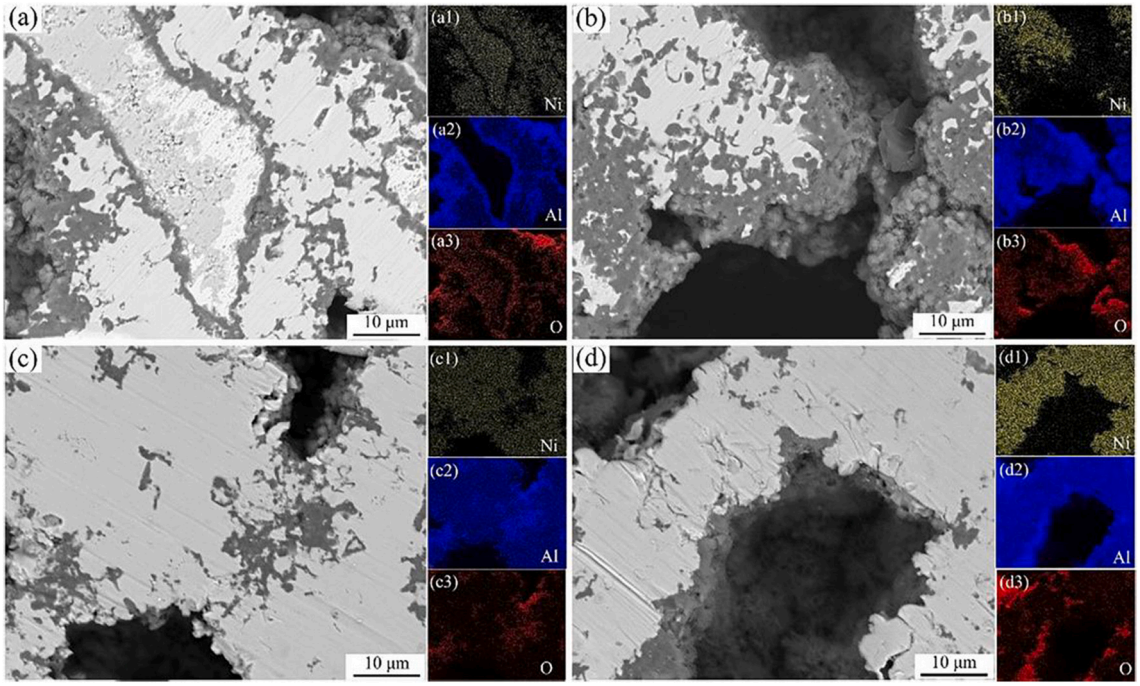

Fig. 17. SEM and EDS images of the cross-section morphology of the oxidized products. (a)-(d) the oxidation product of OS-2, OS-5, OS-10 and OS-20. (a1-d3) mapping distribution of overall elements.

mechanical properties were discussed. Particularly, the pore distribution, phase composition, and permeability of porous NiAl at different heating rates were analyzed by 3D-XRM. The conclusions of this work could be summarized:

(1) TE reaction can be effectively inhibited by reducing the heating rate, and the melting and deformation of porous NiAl can be suppressed. A high heating rate can promote TE reaction, yielding more uniform products. The total porosity of porous NiAl increases with the increasing of the heating rate (2–10 °C min^{-1}).

(2) In the oxidation process, the sample obtained at 20 °C min^{-1} has a uniform phase composition, which shows excellent high-temperature oxidation resistance at 900 °C. The minimum mass gain of the porous NiAl is 3.87%.

(3) 10 °C min^{-1} is the optimal heating rate for NiAl alloy to obtain the best performance compared to the other tested heating rates in this work, offering the porous NiAl with the highest porosity and the highest permeability, which are 57.31% and 2434.6 md, respectively.

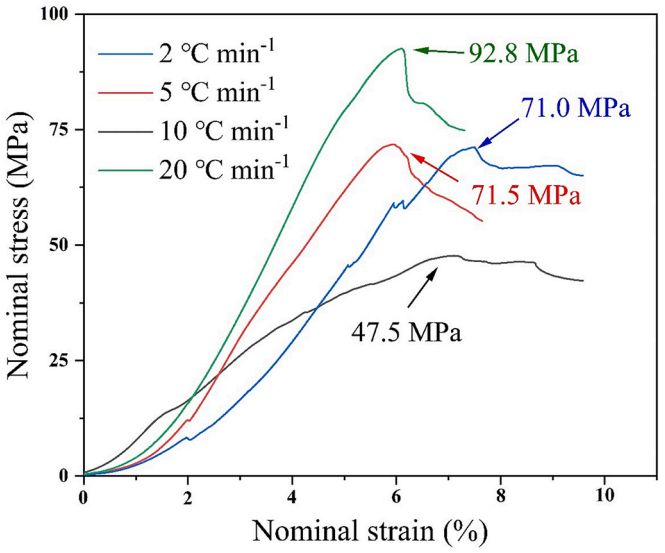

Fig. 18. Compression curves analysis of NiAl compacts with different heating rates.

Supplementary data to this article can be found online at https://doi.org/10.1016/j.matchar.2022.112062.

Data availability

The raw/processed data required to reproduce these findings cannot be shared at this time as the data also forms part of an ongoing study.

CRediT authorship contribution statement

Yang Yu: Data curation, Formal analysis, Visualization, Writing – original draft. **Xiaoping Cai:** Conceptualization, Methodology, Supervision. **Zhejian Cao:** Writing – review & editing. **Xinyang Jiao:** Conceptualization, Methodology, Supervision, Writing – review & editing. **Weining Xie**: Investigation. **Yong Yu:** Investigation. **Peizhong Feng:** Conceptualization, Funding acquisition, Methodology, Supervision.

Declaration of Competing Interest

The authors declared that they have no conflicts of interest to this work. We declare that we do not have any commercial or associative interest that represents a conflict of interest in connection with the work submitted.

Acknowledgments

This research was financially supported by the National Natural Science Foundation of China (No. 52020105011), the Postgraduate Research & Practice Innovation Program of Jiangsu Province (KYCX21_2404) and (KYCX22_2519), the Graduate Innovation Program of China University of Mining and Technology (2022WLJCRCZL274). We are grateful to the Advanced Analysis & Computation Center of China University of Mining and Technology.

References

[1] T.S. Ogneva, I.A. Bataev, V.I. Mali, A.G. Anisimov, D.V. Lazurenko, A.I. Popelyukh, Y.Y. Emurlaeva, A.A. Bataev, S. Tanaka, K.D. Yegoshin, Effect of sintering pressure and temperature on structure and properties of Ni-Al metal-intermetallic composites produced by SPS, Mater. Charact. 180 (2021), 111415.
[2] G. Chen, K.D. Liss, C. Chen, Y.H. He, X.H. Qu, P. Cao, Porous FeAl alloys via powder sintering: phase transformation, microstructure and aqueous corrosion behavior, J. Mater. Sci. Technol. 86 (2021) 64–69.
[3] Y. Jiang, Y.H. He, H.Y. Gao, Recent progress in porous intermetallics: synthesis mechanism, pore structure, and material properties, J. Mater. Sci. Technol. 74 (2021) 89–104.
[4] J.T. Zhang, Z. Zhang, Y.J. Yao, X.Z. Ma, Y.B. Yang, Y. Chen, Z.D. Cheng, In situ construction of Ni enriched porous NiAl as long-lived electrode for hydrogen evolution at high current densities, Appl. Surf. Sci. 489 (2019) 435–445.
[5] X.P. Cai, X.R. Ren, C.C. Sang, L. Zhu, Z.J. Li, P.F. Feng, Dissimilar joining mechanism, microstructure and properties of Ni to 316 stainless steel via Ni-Al thermal explosion reaction, Mat Sci Eng A. 807 (2021), 140868.
[6] M. Seyring, F. Wanierke, T. Kaaden, S. Lippmann, M. Rettenmayr, Influence of natural oxide layers at Ni/NiAl interfaces on Ni3Al phase formation, Mater. Charact. 174 (2021), 111032.
[7] J. Morgiel, O. Poliarus, M. Pomorska, Ł. Maj, M. Szlezynger, Thermal stability of plasma-sprayed NiAl/CrB2composite coatings investigated through in-situ TEM heating experiment, Mater. Charact. 159 (2020), 110068.
[8] M. Jain, S.P. Gupta, Formation of intermetallic compounds in the Ni–Al–Si ternary system, Mater. Charact. 51 (2003) 243–257.
[9] N. Takata, K. Uematsu, M. Kobashi, Compressive properties of porous Ti-Al alloys fabricated by reaction synthesis using a space holder powder, Mater. Sci. Eng. A 697 (2017) 66–70.
[10] G.L. Hao, Q.P. Xu, H. Wang, X.Y. Li, Effect of pore structure on mechanical properties of porous TiAl, mater, Sci. Technol. 32 (2016) 1592–1596.
[11] M. Łazińska, T. Durejko, S. Lipiński, W. Polkowski, T. Czujko, R.A. Varin, Porous graded FeAl intermetallic foams fabricated by sintering process using NaCl space holders, Mater. Sci. Eng. A 636 (2015) 407–414.
[12] S.H. Kayani, N.K. Park, Effect of Cr and Nb on the phase transformation and pore formation of Ti-Al base alloys, J. Alloys Compd. 708 (2017) 308–315.
[13] M.R. Chen, Y. Jiang, Y.H. He, L.W. Lin, B.Y. Huang, C.T. Liu, Pore evolution regulation in synthesis of open pore structured Ti-Al intermetallic compounds by solid diffusion, J. Alloys Compd. 521 (2012) 12–15.
[14] Y.H. Wang, J.P. Lin, Y.H. He, C.K. Zu, G.L. Chen, Pore structures and thermal insulating properties of high Nb containing TiAl porous alloys, J. Alloys Compd. 492 (2010) 213–218.
[15] H.Q. Che, Q.C. Fan, Microstructural evolution during the ignition/quenching of pre-heated Ti/3Al powders, J. Alloys Compd. 475 (2009) 184–190.
[16] M. Adeli, S.H. Seyedein, M.R. Aboutalebi, M. Kobashi, N. Kanetake, A study on the combustion synthesis of titanium aluminide in the self-propagating mode, J. Alloys Compd. 497 (2010) 100–104.
[17] A. Biswas, S.K. Roy, Comparison between the microstructural evolutions of two modes of SHS of NiAl: key to a common reaction mechanism, Acta Mater. 52 (2004) 257–270.
[18] Y.M. Shu, A. Suzuki, N. Takata, M. Kobashi, Fabrication of porous NiAl intermetallic compounds with a hierarchical open-cell structure by combustion synthesis reaction and space holder method, J. Mater. Process. Technol. 264 (2019) 182–189.
[19] H. Sina, S. Iyengar, Reactive synthesis and characterization of titanium aluminides produced from elemental powder mixtures, J. Therm. Anal. Calorim. 122 (2015) 689–698.
[20] John J. Moore, D.W. Readey, H.J. Feng, K. Monroe, B. Mishra, Combustion synthesis of advanced materials: part I, JOM-US 39 (1995) 243–273.
[21] A. Maznoy, A. Kirdyashkin, V. Kitler, A. Solovyev, Combustion synthesis and characterization of porous Ni-Al materials for metal-supported solid oxide fuel cells application, J. Alloys Compd. 697 (2017) 114–123.
[22] R. Rosa, P. Veronesi, A. Casagrande, C. Leonelli, Microwave ignition of the combustion synthesis of aluminides and field-related effects, J. Alloys Compd. 657 (2016) 59–67.
[23] X.P. Cai, Y.N. Liu, P.Z. Feng, X.Y. Jiao, L.Q. Zhang, J.Z. Wang, Fe-Al intermetallic foam with porosity above 60% prepared by thermal explosion, J. Alloys Compd. 732 (2018) 443–447.
[24] Y. Liu, Y.X. Li, F. Li, H. Cui, L.F. Zhang, S.W. Guo, Synthesis and microstructure of Ti2AlN ceramic by thermal explosion, Ceram. Int. 43 (2017) 13618–13621.
[25] M.L. Busurina, L.M. Umarov, I.D. Kovalev, N.V. Sachkova, S.M. Busurin, S. G. Vadchenko, Ti-Al-Nb alloys by thermal explosion: synthesis and characterization, Int J Self-Propag High-Temp Synth. 25 (2016) 92–96.
[26] Z.W. Yang, K.B. Sun, J. Lian, X.Q. Cai, Y. Wang, D.P. Wang, Y.C. Liu, Interfacial microstructure evolution and mechanical properties of Ni3Al-based alloy TLP joints with BNi-2 interlayer, Intermetallics. 125 (2020), 106885.
[27] M. Kobashi, R.X. Wang, Y. Inagaki, N. Kanetake, Effects of processing parameters on pore morphology of combustion synthesized Al-Ni foams, Mater. Trans. 47 (2006) 2172–2177.
[28] K. Morsi, T. Fujii, H. McShane, M. McLean, Control of heat generation during reaction synthesis, Scripta Mater. 40 (1999) 359–364.
[29] X.P. Cai, P.Z. Feng, Reaction mechanism and oxidation resistance at 700–900 °C of high porosity NiAl intermetallic, Corros. Sci. 191 (2021), 109731.
[30] H. Jiang, S.L. Ye, R. Ma, P. Yu, Influences of sintering parameters on shape-retention ability of porous Ni3Al intermetallic fabricated by powder metallurgy, Intermetallics. 105 (2019) 48–55.
[31] X.Y. Jiao, X.R. Ren, X.H. Wang, S.G. Wang, P.Z. Feng, J.Z. Wang, Porous TiAl3 intermetallics with symmetrical graded pore-structure fabricated by leaching space holder and thermal explosion process, Intermetallics. 95 (2018) 144–149.
[32] L.P. Yu, Y. Jiang, Y.H. He, X.L. Liu, H.B. Zhang, Fabrication of porous nickel–copper alloy with controlled micro-sized pore structure through the Kirkendall effect, Mater. Chem. Phys. 163 (2015) 355–361.
[33] J. Sienkiewicz, S. Kuroda, R.M. Molak, H. Murakami, H. Araki, S. Takamori, K. J. Kurzyd1owski, Fabrication of TiAl intermetallic phases by heat treatment of warm sprayed metal precursors, Intermetallics 49 (2014) 57–64.

[34] X.Y. Jiao, P.Z. Feng, J.Z. Wang, X.R. Ren, F. Akhtar, Exothermic behavior and thermodynamic analysis for the formation of porous TiAl3 intermetallics sintering with different heating rates, J. Alloys Compd. 811 (2019), 152056.
[35] G.Y. Yu, H.M. Wang, S.H. Chen, L. Wei, J.H. Huang, J. Yang, Z.Y. Zhao, Interfacial reaction between solid Ni and liquid Al in tens of seconds: dissolution kinetics of solid Ni and formation of intermetallic compounds, Mater. Charact. 159 (2020), 110043.
[36] H.Y. Lee, A. Ikenaga, S.H. Kim, K.B. Kim, The effects of induction heating rate on properties of NieAl based intermetallic compound layer coated on ductile cast iron by combustion synthesis, Intermetallics. 15 (2007) 1050–1056.
[37] X.Y. Jiao, Y.N. Liu, X.P. Cai, J.Z. Wang, P.Z. Feng, Progress of porous Al-containing intermetallics fabricated by combustion synthesis reactions: a review, J. Mater. Sci. 56 (2021) 11605–11630.
[38] C. Gillen, A. Garner, A. Plowman, C.P. Race, T. Lowe, C. Jones, K.L. Moore, P. Frankel, Advanced 3D characterisation of iodine induced stress corrosion cracks in zirconium alloys, Mater. Charact. 141 (2018) 348–361.
[39] S. Bakkar, S. Thapliyal, N. Ku, D. Berman, S.M. Aouadi, R.E. Brennan, M.L. Young, Controlling anisotropy of porous B4C structures through magnetic field-assisted freeze-casting, Ceram. Int. 48 (2022) 6750–6757.
[40] S.Q. Sun, Y. Fang, L. Zhang, C.L. Li, S.Q. Hu, Effects of aging treatment and peripheral coarse grain on the exfoliation corrosion behaviour of 2024 aluminium alloy using SR-C, J Mater Res Technol. 9 (2020) 3219–3229.
[41] L. Yu, Q.D. Hu, Z.Y. Ding, F. Yang, W.Q. Lu, N.F. Zhang, S. Cao, J.G. Li, Effect of cooling rate on the 3D morphology of the proeutectic Al3Ni intermetallic compound formed at the Al/Ni interface after solidification, J. Mater. Sci. Technol. 69 (2021) 60–68.
[42] R. Sarvesha, J. Bhagyaraj, S. Bhagavath, S. Karagadde, J. Jain, S.S. Singh, 2D and 3D characteristics of intermetallic particles and their role in fracture response of AZ91 magnesium alloy, Mater. Charact. 171 (2021), 110733.
[43] Y.H. He, Y. Jiang, N.P. Xu, J. Zou, B.Y. Huang, C.T. Liu, P.K. Liaw, Fabrication of Ti–Al Micro/ nanometer-sized porous alloys through the Kirkendall effect, Adv. Mater. 19 (2007) 2102–2106.
[44] H.B. Zhang, H.Y. Gao, X.L. Liu, H. Yu, L.F. Wang, Y. Jiang, L. Gao, L.P. Yu, Y.H. He, X.M. Chen, L. Zhang, G.Q. Zheng, Reactive synthesis and assessment of porous Fe-20.5Al-18Cr intermetallic material: a comparative study with porous FeCrAl material produced from prealloyed powders, Sep. Purif. Technol. 220 (2019) 152–161.
[45] J.W. Lee, S.K. Hyun, M.S. Kim, M.G. Kim, T. Ide, H. Nakajima, Elevated temperature compression behaviors of lotus-type porous NiAl, Intermetallics. 29 (2012) 27–34.
[46] O.O. Ayodele, M.A. Awotunde, A.O. Adegbenjo, M.B. Shongwe, B.A. Obadele, P. A. Olubambi, Synthesis and heating rate effect on the mechanical properties of NiAl intermetallic compound, Mater. Today 28 (2020) 785–788.
[47] C.P. Zhang, K.F. Zhang, Dependence of heating rate in PCAS on microstructures and high temperature deformation properties of g-TiAl intermetallic compounds, J. Alloys Compd. 492 (2010) 236–240.